*Kovove Mater. 63 2025 309–314*
*DOI: 10.31577/km.2025.5-6.309*


# Microstructural and textural study in Zr-Sn-Nb-Fe-V alloy under different annealing temperatures

Ali Wafaa Aldeen[1]*, Dina Yousif Mahdi[1]

[1] *Department of Materials Engineering, College of Engineering, University of Kufa, Najaf, Iraq*

Received 11 October 2025, received in revised form 6 December 2025, accepted 9 December 2025

**Abstract**

The effects of annealing temperature on the microstructure and texture of the Zr-Sn--Nb-Fe-V alloy were studied using metallographic observation, second-phase particle (SPP) analysis, and texture analysis. The results show that as the annealing temperature following $\beta$-quenching increases, the grain size in the metallographic structure of the Zr-Sn-Nb-Fe--V sheet gradually increases, and the average size and size distribution range of the SPPs gradually increase. The Zr-Sn-Nb-Fe-V sheets at various annealing temperatures all have {0001} basal texture, and the texture strength of the sheets at different annealing temperatures varies significantly.

K e y w o r d s: Zr-Sn-Nb-Fe-V alloy, annealing temperature, metallographic structure, second phase particles, texture

## 1. Introduction

Zirconium alloys are often used as fuel cladding and structural materials for water-cooled reactors in nuclear power plants due to their low thermal-neutron absorption cross-sections and excellent corrosion resistance [1]. Zr-2 alloys have been maturely used in boiling water reactors (BWRs), and Zr-4 alloys have been widely used in pressurized water reactors (PWRs). With the continuous growth in electricity demand in my country, people have raised their requirements for fuel consumption and nuclear reactor power. The Nb element not only has a low thermal-neutron absorption cross-section but can also offset the harmful effects of impurities such as carbon, nitrogen, aluminum, and titanium on the corrosion resistance of zirconium alloys. At the same time, it can also effectively reduce the amount of hydrogen absorbed by zirconium alloys. Consequently, many countries worldwide are developing new, high-performance zirconium alloys. Zr-Sn-Nb-Fe alloys are a key area of continuous improvement for zirconium alloys used in PWR high-burnup assemblies [1–4]. Zr-Sn-Nb-Fe alloys containing V have demonstrated excellent in-pile corrosion resistance. For example, the US X1 (Zr-0.3Sn-0.7Nb--0.05Fe-0.12Cu-1.2V) alloy has a maximum oxide film thickness of less than 50 $\mu m^2$ when tested in a pressurized water reactor nuclear power plant at a burnup of equal to or more than 70 GWd/MTU, which can meet the design requirements of high burnup and long-life fuel element cladding materials for pressurized water reactors and is a fuel element cladding material with outstanding potential. V-containing zirconium alloys are very sensitive to heat treatment and require extensive heat treatment to achieve excellent corrosion resistance. Currently, there are few reports discussing the relationship between the annealing temperature after $\beta$-solution treatment and the evolution of microstructure and texture in Zr-Sn-Nb-Fe-V alloys [5–10]. This study investigates the recrystallization, SPPs, and grain orientation behavior of a Zr-0.4Sn--0.12Nb-0.3Fe-0.2V alloy sheet after annealing at different temperatures. We also analyzed how annealing temperature affects SPP size.

## 2. Experimental materials and methods

The historical reference process for preparing the Zr-0.4Sn-0.12Nb-0.3Fe-0.2V alloy sheet includes a se-

*Corresponding author: e-mail address: aliw.altalqani@uokufa.edu.iq

ries of steps: vacuum consumable arc melting of ingots, ingot forging, $\beta$-phase homogenization and water quenching, 600 ℃ hot extrusion, four-pass cold rolling, and intermediate and final annealing. The as-received sheet (from China) was cut into a group of 10 mm × 10 mm × 1 mm samples. Firstly, all samples were subjected to $\beta$ solution treatment at 1030 ℃ for 50 min, followed by quenching in cold water. Before the experiment, the $\beta$-quenched samples were cleaned with anhydrous ethanol and deionized water, then placed in a vacuumed tubular heating furnace, where the temperature was raised at a constant rate. The temperature was kept at 500, 600, and 700 ℃ for 6 hours. The annealed specimens were gradually polished using 200- to 5000-grit sandpaper. The specimens were then etched in a mixed acid solution (45 % $H_2O$, 45 % $HNO_3$, and 10 % HF) and sprayed with a hair dryer. The grain size of each annealed sample was then observed using a metallographic microscope. SPPs were observed using an FESEM microscope. Finally, quantitative metallography and *Image analysis software* (*ImageJ*) were used to analyze the average size and size distribution of the SPPs in each sample. At least 200 SPPs were counted for each sample. Grain boundary and texture analysis were performed using a scanning electron microscope equipped with an electron backscatter diffraction (EBSD) detector.

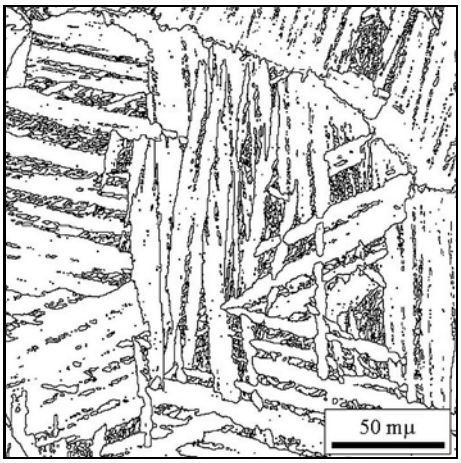


Fig. 1. EBSD of $\beta$-quenched sheet samples.

## 3. Results and discussion

### *3.1. Effect of β-solution treatment*

Figure 1 shows the EBSD grain orientation image of the Zr-0.4Sn-0.12Nb-0.3Fe-0.2V alloy sheet after $\beta$-solution treatment. As shown in Fig. 1, the growth patterns of the $\alpha$-plates were characterized by the conversion of the high-temperature $\beta$ phase into a Widmanstätten interlaced $\alpha$-plate structure with var-

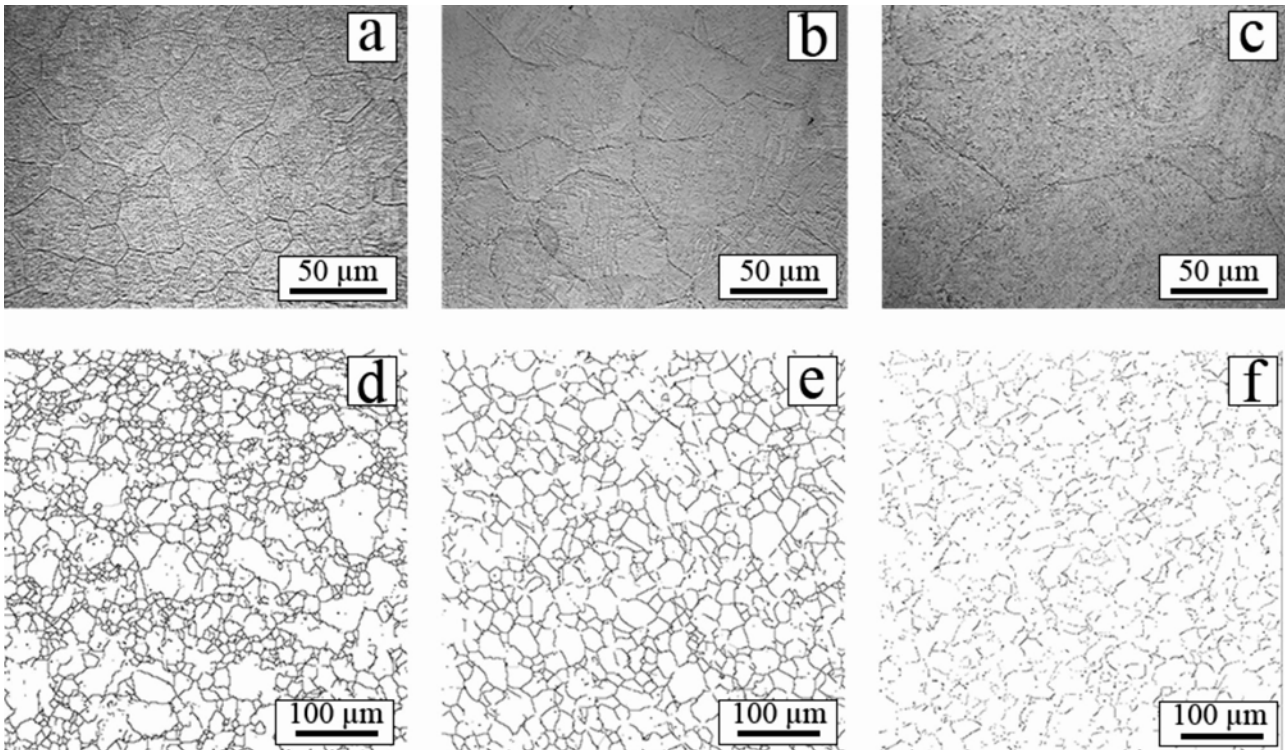


Fig. 2. Microstructure of Zr-0.4Sn-0.12Nb-0.3Fe-0.2V alloy samples with different annealing temperatures: (a) and (d) 500 ℃/6 h, (b) and (e) 600 ℃/6 h, (c) and (f) 700 ℃/6 h. Note that (a)–(c) optical microscope examination and (d)–(f) EBSD examination.

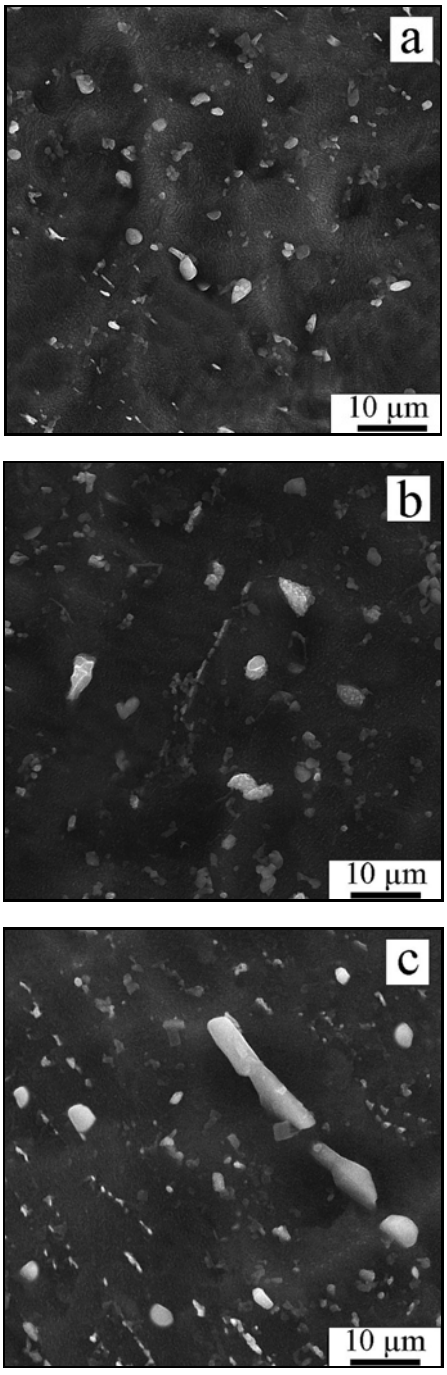


Fig. 3 SEM-SE images of the SPPs in Zr-0.4Sn-0.12Nb--0.3Fe-0.2V alloy samples annealed at different temperatures (a) 500 °C/6 h, (b) 600 °C/6 h, and (c) 700 °C/6 h.

ious crystallographic orientations, encircled by previous $\beta$-grain boundaries.

### *3.2. Effect of annealing temperature following β-treatment on the metallographic structure of the sample*

Figure 2 shows the effect of annealing temperatures on both the grain growth and the grain boundaries of

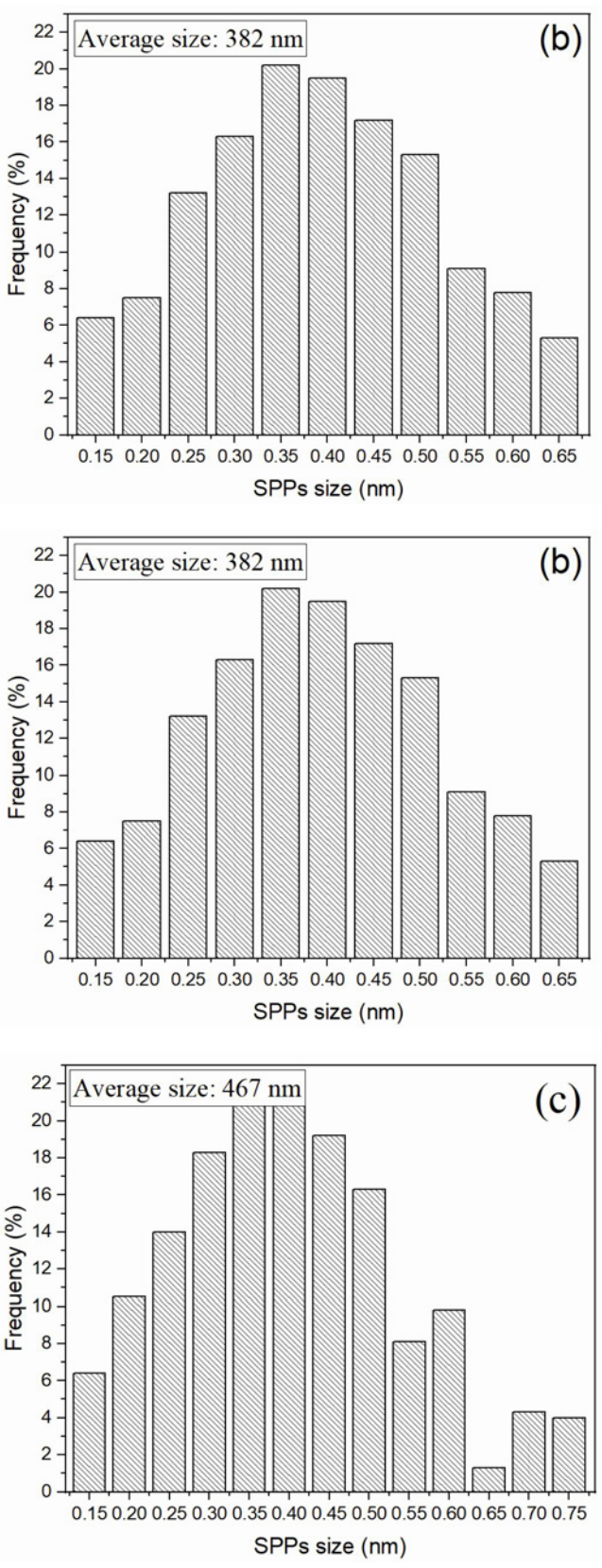


Fig. 4. Particle size distribution of the SPPs in Zr--0.4Sn-0.12Nb-0.3Fe-0.2V alloy samples annealed at different temperatures: (a) 500 °C/6 h, (b) 600 °C/6 h, and (c) 700 °C/6 h.

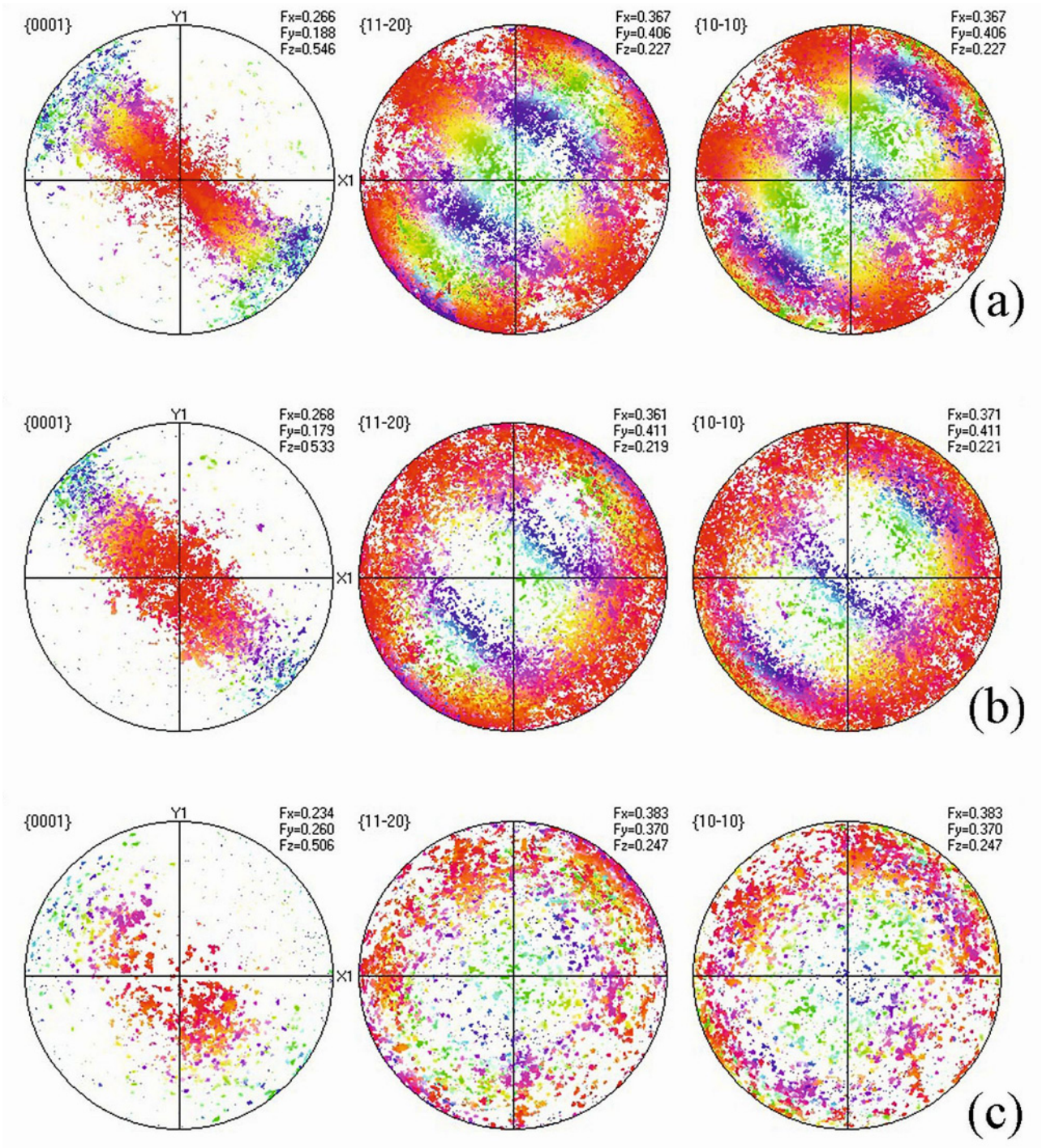


Fig. 5. EBSD pole figure images of Zr-0.4Sn-0.12Nb-0.3Fe-0.2V samples annealed at different temperatures: (a) 500 ℃/6 h, (b) 600 ℃/6 h, and (c) 700 ℃/6 h.

annealed samples. After annealing at 500 ℃/6 h, the interlaced $\alpha$-plates almost disappeared and changed to a high percentage of fine and distinct recrystallized grain structure, as shown in Figs. 2a,d, which, in turn, consumed the high energy conserved during the quenching after the $\beta$-treatment process and used it as a driving force for recrystallization. As the annealing temperature rose to 600 ℃/6 h, the effect of increasing temperature was clearly evident in recrystallization and granular growth, as shown in Figs. 2b,e. Finally, after annealing at 700 ℃/6 h, the grains grow significantly, sometimes with massive ones, and exhibit a certain degree of directionality.

This trend is consistent with changes in the grain structure of conventional Zr-Sn-Nb alloy sheets (which have relatively high levels of impurities such as C and

N) with increasing annealing temperature [2, 11–14].

### 3.3. Effect of annealing temperature on the size of the second-phase particles

Figure 3 is the SEM-SE image of the SPPs of each annealed sample. Figure 4 displays the statistical outcome of the SPPs' size distribution. As shown in Fig. 3a and Fig. 4a, after annealing at 500 ℃/6 h, the size of the SPPs in the Zr-0.4Sn-0.12Nb-0.3Fe-0.2V sample ranges from 0.10 to 0.60 μm, and the particles show random distribution, with an average size of 0.315 μm. After annealing at 600 ℃/6 h, as shown in Fig. 3b and Fig. 4b, the size of the SPPs in the Zr-0.4Sn-0.12Nb-0.3Fe-0.2V sample gradually increased and ranged from 0.15 to 0.65 μm, with an average size of 0.382 μm, with some irregularly shaped particles. Figures 3c and 4c show that after annealing at 700 ℃ for 6 h, the SPP size in the alloy sample ranges from 0.15 to 0.75 μm, with an average of 0.467 μm.

This evidence indicates that the average size and size distribution of the SPPs in the alloy increase significantly with increasing annealing temperature [15, 16]. The irregular shape of particles also increased, indicating that, with increasing annealing temperatures, the particle size follows the Ostwald ripening mechanism [17, 18].

### 3.4. Effect of annealing temperature on the sample's texture

Figure 5 displays EBSD pole figure maps for the Zr-0.4Sn-0.12Nb-0.3Fe-0.2V samples at various annealing temperatures. As can be seen from Figs. 5a–c, the Zr-0.4Sn-0.12Nb-0.3Fe-0.2V alloy samples at different annealing temperatures have a {0001} basal texture, and the texture strength of the samples at 500 ℃/6 h and 600 ℃/6 h annealing temperatures is slightly different. These differences may be related to the processing method of the sheet during cold rolling and the directional growth of the grains in the Zr-0.4Sn-0.12Nb-0.3Fe-0.2V samples after the annealing process, because the new strain-free grains nucleate and most of the recovery occurs in addition to the driving force still not being a big difference during this range of temperatures [19–21].

At 700 ℃/6 h, the temperature surpasses the onset of full recrystallization, causing new strain-free grains to nucleate with various crystallographic orientations. Boundary mobility increases, allowing favourable orientations to grow at the expense of others, thereby significantly altering the texture. Additionally, at this annealing temperature, the stored energy is completely available to facilitate recrystallization and orientation selection, resulting in substantial reorientation [22–24].

## 4. Conclusions

1. With an increase in annealing temperature, the grain size in the metallographic structure of the Zr-0.4Sn-0.12Nb-0.3Fe-0.2V sheet samples gradually increases and shows a certain directionality.

2. With the increase of annealing temperature, the average size and size distribution range of the SPPs in the Zr-0.4Sn-0.12Nb-0.3Fe-0.2V sheet samples gradually increase between 500 ℃/6 h and 600 ℃/6 h and significantly increase at 700 ℃/6 h.

3. The Zr-0.4Sn-0.12Nb-0.3Fe-0.2V alloy sheets annealed at different temperatures all have {0001} basal texture, and the texture strength of the alloy sheets annealed at different temperatures is slightly different between 500 ℃/6 h and 600 ℃/6 h and quite different at 700 ℃/6 h.

## Acknowledgements

The authors gratefully acknowledge Baoji Five Elements Metal Co., Ltd, for the Zr alloy sheet. Special thanks to Mr Erik Nilsson for his cooperation in this work.

## References

[1] A. W. Aldeen, Z. W. Chen, I. A. Disher, M. Samiuddin, K. Yan, Second phase particles in Zr–Sn–Nb–Fe alloys: A review, Phys. Met. Metallogr. 124 (2023) 362–379. https://doi.org/10.1134/S0031918X22601470

[2] W. Liu, Q. Li, B. Zhou, Q. Yan, M. Yao, Effect of heat treatment on the microstructure and corrosion resistance of a Zr–Sn–Nb–Fe–Cr alloy, J. Nucl. Mater. 341 (2025) 97–102. https://doi.org/10.1016/j.jnucmat.2005.01.007

[3] Y. Z. Liu, X. T. Zu, S. Y. Qiu, C. Li, W. G. Ma, X. Q. Huang, Surface characteristics and oxidation behavior of nitrogen ion-implanted Zr–Sn–Nb alloy, Surf. Coatings Technol. 200 (2006) 5631–5635. https://doi.org/10.1016/j.surfcoat.2005.07.103

[4] J. Liu, Y. Liu, A.-L. Deng, H. Chen, Z.-Q. Cheng, L. Zhang, Phase transition temperature and non-isothermal kinetics in zirconium alloys by differential scanning calorimetry, Mater. Express 13 (2023) 87–394. https://doi.org/10.1166/mex.2023.2332

[5] X. Wang, J. Li, Z. Zhao, Y. Yu, H. Shi, Corrosion behaviors of Zr-Sn-Nb alloys: Influence of different concentration dissolved oxygen environment and trace V element on the anti-corrosion properties, J. Nucl. Mater. 595 (2024) 155068. https://doi.org/10.1016/j.jnucmat.2024.155068

[6] Q. Fan, B. Yuan, M. Xie, M. Shi, J. Zhou, Z. Yang, W. Zhao, Effects of hot rolling temperature and aging on the second phase particles of Zr-Sn-Nb-Fe zirconium alloy, Nucl. Mater. Energy 20 (2019) 100700. https://doi.org/10.1016/j.nme.2019.100700

[7] A. M. Garde, R. J. Comstock, G. Pan, R. Baranwal, L. Hallstadius, T. Cook, F. Carrera, Advanced zirconium alloy for PWR application, In: Zirconium

in the Nuclear Industry: 16th International Symposium, ASTM International, 2010, pp. 784–800. https://doi.org/10.1520/JAI103030
[8] M. Isaenkova, O. Krymskaya, K. Klyukova, A. Bogomolova, I. Kozlov, P. Dzhumaev, V. Fesenko, R. Svetogorov, Regularities of changes in the structure of different phases of deformed zirconium alloys as a result of raising the annealing temperature according to texture analysis data, Metals (Basel) 13 (2023) 1784. https://doi.org/10.3390/met13101784
[9] Y. Tang, J. Liao, D. Yun, Understanding the high-temperature corrosion behavior of zirconium alloy as cladding tubes: A review, Front. Mater. 11 (2024) 1–14. https://doi.org/10.3389/fmats.2024.1381818
[10] S. Y. Betsofen, E. F. Volkova, A. A. Shaforostov, Effect of alloying elements on the formation of rolling texture in Mg-Nd-Zr and Mg-Li alloys, Russ. Metall. 2011 (2011) 66–71. https://doi.org/10.1134/S0036029511010058
[11] Y. Il Jung, M. H. Lee, H. G. Kim, J. Y. Park, Y. H. Jeong, Behavior of a recrystallization in HANA-4 and HANA-6 zirconium-based alloys, J. Alloys Compd. 479 (2009) 423–426. https://doi.org/10.1016/j.jallcom.2008.12.089
[12] T. Wei, X. Dai, Ch. Long, Ch. Sun, S. Long, J. Zheng, P. Wang, Y. Jia, J. Zhang, Comparison on the microstructure, aqueous corrosion behavior and hydrogen uptake of a new Zr-Sn-Nb alloy prepared by different hot rolling temperature, Corros. Sci. 192 (2021) 109808. https://doi.org/10.1016/j.corsci.2021.109808
[13] R. Tewari, D. Srivastava, G. K. Dey, J. K. Chakravarty, S. Banerjee, Microstructural evolution in zirconium based alloys, J. Nucl. Mater. 383 (2008) 153–171. https://doi.org/10.1016/j.jnucmat.2008.08.041
[14] Y. Jia, Z. Wu, X. Dai, W. Yi, Effect of microstructure variation induced by processing on corrosion behavior of Zr-Sn-Nb alloy, J. Nucl. Mater. 603 (2024) 155418. https://doi.org/10.1016/j.jnucmat.2024.155418
[15] H. Shi, X. Guo, J. Li, J. Mao, W. Lu, Effects of Mn addition on the corrosion behaviors of Zr-Sn-Nb-Fe-Mo alloys, Corros. Sci. 157 (2019) 167–179. https://doi.org/10.1016/j.corsci.2019.06.002
[16] B. D. C. Bell, S. T. Murphy, P. A. Burr, R. J. Comstock, J. M. Partezana, R. W. Grimes, M. R. Wenman, The influence of alloying elements on the corrosion of Zr alloys, Corros. Sci. 105 (2016) 36–43. https://doi.org/10.1016/j.corsci.2015.12.022
[17] P. W. Voorhees, The theory of Ostwald ripening, J. Stat. Phys. 38 (1985) 231–252. https://doi.org/10.1007/BF01017860
[18] B. M. Jenkins, J. Haley, M. P. Moody, J. M. Hyde, C. R. M. Grovenor, APT and TEM study of behaviour of alloying elements in neutron-irradiated zirconium-based alloys, Scr. Mater. 208 (2022) 114323. https://doi.org/10.1016/j.scriptamat.2021.114323
[19] Y. Cao, T. Wu, L. Xia, P. Feng, C. Jiang, D. Chen, The role of primary $\alpha$ grains in the degree of transformation texture obeying the Burgers orientation relationship in Zr alloys, Int. J. Refract. Met. Hard Mater. 107 (2022) 105908. https://doi.org/10.1016/j.ijrmhm.2022.105908
[20] H. R. Wenk, I. Lonardelli, D. Williams, Texture changes in the hcp $\rightarrow$ bcc $\rightarrow$ hcp transformation of zirconium studied in situ by neutron diffraction, Acta Mater. 52 (2004) 1899–1907. https://doi.org/10.1016/j.actamat.2003.12.029
[21] K. L. Murty, I. Charit, Texture development and anisotropic deformation of zircaloys, Prog. Nucl. Energy 48 (2006) 325–359. https://doi.org/10.1016/j.pnucene.2005.09.011
[22] H. Shi, X. Guo, J. Li, J. Mao, J. Lu, W. Lu, Variation of microstructural features on the tensile property and corrosion resistance of Zr-Sn-Nb-Fe-Cu alloy, Mater. Charact. 151 (2018) 84–95. https://doi.org/10.1016/j.matchar.2019.02.043
[23] C. S. Daniel, P. D. Honniball, L. Bradley, M. Preuss, J. Quinta da Fonseca, A detailed study of texture changes during alpha–beta processing of a zirconium alloy, J. Alloys Compd. 804 (2019) 65–83. https://doi.org/10.1016/j.jallcom.2019.06.338
[24] A. C. Souza, F. Aristone, J. L. Rossi, L. G. Martinez, F. C. Cione, P. Tsakiropoulos, C. R. Grandini, W. F. da Silva, Microstructural characterization of Zr1Nb alloy after hot rolling, Int. J. Refract. Met. Hard Mater. 80 (2019) 216–224. https://doi.org/10.1016/j.ijrmhm.2018.12.015